CHEMISTRY
A EUROPEAN JOURNAL

FULL PAPER

DOI: 10.1002/chem.201302992

Ultrafast Deactivation Mechanism of the Excited Singlet in the Light-Induced Spin Crossover of $[Fe(2,2'\text{-bipyridine})_3]^{2+}$

Carmen Sousa,[b] Coen de Graaf,*[a, c, d] Andrii Rudavskyi,[d] Ria Broer,[d] Jörg Tatchen,[e] Mihajlo Etinski,[f] and Christel M. Marian[e]

Abstract: The mechanism of the light-induced spin crossover of the $[Fe(bpy)_3]^{2+}$ complex (bpy = 2,2′-bipyridine) has been studied by combining accurate electronic-structure calculations and time-dependent approaches to calculate intersystem-crossing rates. We investigate how the initially excited metal-to-ligand charge transfer (MLCT) singlet state deactivates to the final metastable high-spin state. Although ultrafast X-ray free-electron spectroscopy has established that the total timescale of this process is on the order of a few tenths of a picosecond, the details of the mechanisms still remain unclear. We determine all the intermediate electronic states along the pathway from low spin to high spin and give estimates for the deactivation times of the different stages. The calculations result in a total deactivation time on the same order of magnitude as the experimentally determined rate and indicate that the complex can reach the final high-spin state by means of different deactivation channels. The optically populated excited singlet state rapidly decays to a triplet state with an Fe $d^6(t_{2g}^5 e_g^1)$ configuration either directly or by means of a triplet MLCT state. This triplet ligand-field state could in principle decay directly to the final quintet state, but a much faster channel is provided by internal conversion to a lower-lying triplet state and subsequent intersystem crossing to the high-spin state. The deactivation rate to the low-spin ground state is much smaller, which is in line with the large quantum yield reported for the process.

Keywords: ab initio calculations · electronic structure · iron · magnetic properties · spin crossover

Introduction

Controlling the magnetic properties of transition-metal complexes is one of the key factors in the search for new materials that can eventually be used in technological applications. There are several ways to influence the magnetism by external perturbations such as light, temperature, and magnetic or electric fields.[1,2] A well-known example is formed by the family of single-molecule magnets, the magnetization of which can be inverted from $+M_S$ to $-M_S$ (and vice versa) by the application of an external magnetic field.[3–6] The Prussian blue analogues are a second important example of systems that show magnetic bistability. Shining light on the material can induce the transfer of an electron from one metal site to a neighboring one, thereby generating unpaired electrons in the d orbitals of the transition metals. The resulting spin-angular moments are coupled (anti)ferromagnetically and can lead to a net nonzero magnetization at finite temperature.[7,8] Although Prussian blue analogues are extended materials, the same phenomenon has also been observed in molecular complexes.[9–11]

The spin-crossover phenomenon provides yet another way to attain bistability in molecules. When transition-metal ions of $3d^n$ ($n = 4$–7) electronic configuration are surrounded by groups that exert a weak ligand field, the low-spin configuration with maximum electron pairing might be in competition with the high-spin configuration, in which the number of unpaired d electrons is as large as possible. Most commonly, spin crossover has been observed in Fe^{II} complexes, but other ions and oxidation states can also give rise to nearly degenerate high-spin and low-spin states. Recently, spin crossover has even been detected for Ni^{II} $3d^8$ complexes.[12,13]

The transition between the two configurations is typically induced by changes in temperature or by irradiation with

[a] Dr. C. de Graaf
Departament de Química Física i Inorgànica
Universitat Rovira i Virgili
Marcel-lí Domingo s/n, 43007 Tarragona (Spain)
Fax: (+34)-977559563
E-mail: coen.degraaf@urv.cat

[b] Dr. C. Sousa
Departament de Química Física and Institut de Química
Teòrica i Computacional, Universitat de Barcelona
C/Martí i Franquès 1, 08028 Barcelona (Spain)

[c] Dr. C. de Graaf
Institució Catalana de Recerca i Estudis Avançats (ICREA)
Passeig Lluís Companys 23, 08010 Barcelona (Spain)

[d] Dr. C. de Graaf, A. Rudavskyi, Dr. R. Broer
Zernike Institute for Advanced Materials, University of Groningen
Nijenborgh 4, 9747 AG Groningen (The Netherlands)

[e] Dr. J. Tatchen, Dr. C. M. Marian
Institute of Theoretical and Computational Chemistry
Heinrich-Heine University Düsseldorf
Universitätsstrasse 1, 40225 Düsseldorf (Germany)

[f] Dr. M. Etinski
Faculty of Physical Chemistry, University of Belgrade
Studentski Trg 12–16, 11158 Belgrade (Serbia)

light. The latter case is usually referred to as light-induced excited spin-state trapping (LIESST). If we take a quasi-octahedral Fe^{II} complex as an example, the initial low-spin Fe $3d^6$ state of closed-shell character is excited by promoting an electron to a higher-lying Fe 3d orbital or to an unoccupied ligand orbital, typically of π^* character. This excited ligand-field or metal-to-ligand charge-transfer (MLCT) singlet state decays through various intersystem crossings (ISC) and internal conversions to the metastable high-spin state in which, relative to the initial low-spin state, two electrons are transferred to the antibonding Fe $3d(e_g)$-like orbitals. The occupation of these antibonding orbitals causes an enlargement of the Fe–ligand bond lengths of about 0.2 Å. The lifetime of the high-spin state can vary from nanoseconds[14] to several days.[15] For systems with sufficiently long-lived high-spin states, the low-spin state can also be repopulated through irradiation, thereby giving rise to a switchable material. This reverse LIESST process proceeds through an excited ligand-field quintet state (MLCT states with quintet spin coupling are expected to be very high in energy[16]) and subsequent deactivation to the low-spin closed-shell singlet.

The general features of the mechanism of (reverse) LIESST are well understood and have been described in a review article by Hauser.[17] Nevertheless, the extremely fast deactivation and relatively short lifetime of the metastable high-spin state makes it difficult to obtain detailed information about the mechanism and several questions remain unanswered. Stimulated by recent developments in ultrafast optical and X-ray spectroscopy, new information has become available for some Fe^{II} complexes as $[Fe(bpy)_3]^{2+}$ and $[Fe(phen)_3]^{2+}$ (bpy = 2,2-bipyridine; phen = phenanthroline).[14,18–24] Time-resolved measurements on the former complex in solution showed that the first step in the deactivation takes less than 30 fs and involves a singlet-to-triplet conversion within the MLCT manifold. Subsequently, the system evolves into a vibrationally excited quintet state within 200 fs (see Figure 1). The dissipation of the excess amount of vibrational energy takes place on a picosecond timescale, and the lifetime of the resulting high-spin state was measured to be around 650 ps.[25,26]

Although these measurements gave very valuable information and clarified a large part of the photocycle, there are still some issues that need to be resolved. In the first place, it remains unclear whether other electronic states are involved in the deactivation of the excited singlet or if the system relaxes directly from the ^{3}MLCT into the final high-spin state. Argument in favor of the direct relaxation are the fact that the quintet state is nearly degenerate with the MLCT states in the Franck–Condon region as shown in Figure 1. This could favor a fast and selective conversion, in line with the almost 100% quantum yield. Moreover, X-ray absorption near-edge structure (XANES) measurements were also simulated assuming a path through the triplet ligand-field states. The data could only be fitted with a relaxation time smaller than 60 fs, which was concluded to be unrealistic as it is shorter than the Fe–N vibrational stretching period.[18]

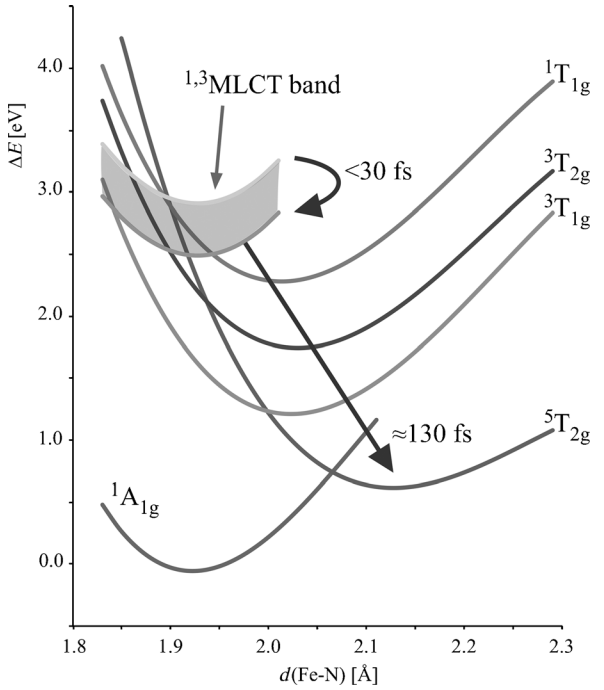

Figure 1. Schematic representation of the potential-energy surfaces of the lowest electronic states of $[Fe(bpy)_3]^{2+}$ as function of the Fe–N distance (based on CASPT2 results from Ref. [16]) and the main experimental findings on the deactivation dynamics. The ligand-field states are labeled according to O_h symmetry.

However, it should be noted that the intersystem crossing (ISC) from triplet to quintet only becomes possible due to the existence of spin–orbit coupling. Given that the overall process takes place on a very small timescale, this coupling should be rather effective. As noted by some of us,[16] the matrix elements of the spin–orbit operator between the M_S components of the ^{3}MLCT and final high-spin state are all very small due to the fact that the electronic configurations of the two states differ by two orbital occupations. Hence, the direct deactivation from ^{3}MLCT to the quintet state seems less probable, despite the fact that the two states are close in energy in the Franck–Condon region.

Moreover, the energy of the triplet ligand-field states is only slightly lower than the MLCT states in the initial geometry of the complex before Fe–N bond elongation. Vibrationally excited triplet ligand-field states might be close enough to enable ISC or internal conversion from $^{(1,3)}$MLCT states to the triplet ligand-field states. This provides a plausible deactivation channel; however, when the relaxation takes place by means of these triplet ligand-field states, it is not easily explained why the light-induced mechanism is so highly selective. A simple look at the schematic Jablonski diagram[27,28] (or the more quantitative ones published recently[29–31]) shows that there is no clear reason for the triplet states to exclusively take the route to the quintet state and not to return to the initial low-spin state.

Finally, it has been suggested in the literature that the change from singlet to triplet to quintet spin-coupled states

might take place entirely in the MLCT manifold.[32,33] This mechanism resolves the high selectivity of the process, since there is no way to escape to the low-spin state once the ^{5}MLCT state is reached. Moreover, the singlet–triplet and triplet–quintet spin–orbit coupling matrix elements are rather large in the MLCT manifold, which favors the possibility of intersystem crossings. However, a major problem is that the lowest ^{5}MLCT states are significantly higher in energy than the MLCT states with lower spin moments. This difference is about 2 eV in the Franck–Condon region.[16] The Fe−N bond elongation lowers this difference but it never becomes less than 1 eV.

To further explain the photocycle of spin-crossover materials, it is desirable to include additional information from theory about the deactivation mechanism. In earlier contributions, we described the energetics and the size of the spin–orbit coupling matrix elements in $[Fe(bpy)_3]^{2+}$. By interpolating between the optimized geometries of the lowest singlet and quintet states, we derived the relative energies of all the electronic states relevant to the deactivation process along an approximate reaction coordinate. This coordinate is basically characterized by the Fe−N bond elongation, but has also included small structural relaxation in the bipyridine ligands to release the strain induced by the displacements of the N atoms. All these calculations were performed in a static framework, and to obtain more specific information about the dynamics of the deactivation, we extended the previous treatments through the calculation of the ISC rates between the relevant electronic states. For this purpose, we have relied on Fermi's golden rule and apply the recently developed time-dependent approach[34] to perform the summation over the vibrational levels. This new method of computing intersystem crossings outperforms the traditional time-independent method[35] for large systems with many vibrational modes, high densities of vibrational final states, or large energy gaps between initial and final states. The $[Fe(bpy)_3]^{2+}$ complex under study here is certainly a case in which the time-independent approach would lead to unfeasibly long computation times to get precise estimates of the ISC rates.

The calculation of ISC rates requires accurate estimates of the energy differences between the electronic states, the spin–orbit coupling matrix elements, and the vibrational frequencies plus the corresponding displacement vectors of the normal modes. The first two ingredients were already calculated in our previous account of the complex and will only be reviewed in brief. On the other hand, the computation of the vibrational states will be described in more detail and followed by a careful analysis of the ISC rates. It will be shown that our computational approach gives an overall deactivation time that is in good agreement with the experimental estimate of approximately 200 fs and that the deactivation by means of ligand-field triplet states can be both fast and selective. Our findings mark the ^{1}MLCT$\rightarrow$(^{3}MLCT$\rightarrow$)$^3T_{2g}\rightarrow{}^3T_{1g}\rightarrow{}^5T_{2g}$ as the most probable deactivation path to explain the light-induced spin-crossover mechanism.

Computational Methods

The theoretical description of the photocycle of the light-induced spin crossover relies on three basic ingredients. In the first place, accurate equilibrium geometries and vibrational frequencies are needed for all the electronic states involved in the deactivation process. Secondly, the relative energies of these states are required, and finally, spin–orbit coupling matrix elements are essential to estimate the intersystem-crossing rates between electronic states of different spin multiplicity.

Unfortunately, so far there has been no computational scheme that can provide accurate estimates for all three ingredients in the transition-metal complex under study here. Density functional theory (DFT) is a very efficient method to obtain good geometries and vibrational frequencies, whereas the precision of the relative energies of the different electronic states is a matter of lively debate in the literature.[36–42] On the other hand, multiconfigurational wavefunction-based approaches give an accurate account of the energies, but geometry optimizations and the calculation of vibrational frequencies are out of reach because of the high computational cost of these methods.

Therefore, we have combined the DFT geometries and vibrational frequencies with relative energies and spin–orbit matrix elements calculated within the CASSCF/CASPT2 approach. DFT calculations were performed with Turbomole 6.3[43,44] using the Perdew–Becke–Ernzerhof (PBE0) hybrid functional[45,46] and the default triplet-ζ plus polarization basis sets (def2-TZVP).[47] The geometry optimizations of the singlet, triplet, and quintet spin states of lowest energy were carried out with the standard spin (un)restricted DFT formalism for ground-state systems, and vibrational frequencies were determined analytically in the harmonic approximation. This is no longer possible for the excited states, and we have used the time-dependent formulation of DFT (TD-DFT) in the random phase approximation.[48–50] The harmonic frequencies were determined numerically in this case. To minimize the numerical noise in these calculations, we have used tight convergence criteria (*rpaconv* = 8, *scfconv* = 8, *denconv* = 1d-7) and fine integration grids (*mgrid* = 6). All DFT calculations were carried out without symmetry restrictions, although the optimized geometries are close to D_3 symmetry, especially for the low-spin (LS) state.

The CASSCF/CASPT2 calculations[51] were carried out as described in previous studies.[16,31] We have used Molcas 7.4[52,53] with an atomic natural orbitals basis set (ANO-RCC) for all atoms.[54] The number of contracted functions in the basis is (7s, 6p, 5d, 4f, 3g, 2h) for Fe, (4s, 3p, 1d) for N, (3s, 2p) for C, and (2s) for H. The active space used to construct the CASSCF wavefunctions contains ten electrons and fifteen orbitals. The active orbitals can be identified as five Fe 3d orbitals, two N σ orbitals that point towards the Fe atom, three ligand orbitals of π* character, and five Fe 3d′ orbitals to deal with the large electron correlation effects in the Fe 3d shell. This is the minimal active space to provide accurate estimates of the relative energies of the different ligand-field and metal-to-ligand charge-transfer states.[38,55,56] CASPT2 correlates all electrons except the deep-core electrons (Fe $1s^2$, $2s^2$, $2p^6$ and (C−N) $1s^2$). We used the standard choice of the zeroth-order Hamiltonian[57] and applied a small level shift (0.15 au) to avoid interference from intruder states.[58] The spin–orbit coupling was accounted for with the state interaction procedure proposed by Malmqvist et al.[59,60] using the atomic mean-field approximation.[61] The spin–orbit matrix elements between the different electronic states were calculated using the CASSCF wavefunctions and CASPT2 energies. In all cases, we imposed the symmetry restrictions of the C_2 point group on the molecular orbitals. To simplify the discussions, the ligand-field states were labeled according to the O_h-symmetry group. This can be justified by the fact that the energy splitting of the components of the different states is small.[62]

The geometries and vibrational frequencies obtained from the DFT calculations combined with the CASPT2 relative energies of the different spin states and the spin–orbit coupling matrix elements are the necessary ingredients for the calculation of the intersystem-crossing rate constants (k_{ISC}) from Fermi's golden rule [Eq. (1)]:

$$k_{ISC} = 2\pi \sum_{k} \left| \left\langle \Phi_I, \{v_{Ia}\} | \hat{H}_{SO} | \Phi_F, \{v_{Fk}\} \right\rangle \right|^2 \delta(E_{Ia} - E_{Fk}) \quad (1)$$

in which $\Phi_{I,F}$ is the initial and final electronic states, respectively, $\{\nu\}$ is the collection of vibrational states, and $\hat{H}_{SO}$ the spin–orbit coupling operator. In the Condon approximation, this equation can be factorized into an electronic and a vibrational part [Eq. (2)]:

$$k_{ISC} = 2\pi \left| \left\langle \Phi_I | \hat{H}_{SO} | \Phi_F \right\rangle \right|^2 \times \sum_{k} |\langle \{v_{Ia}\} | \{v_{Fk}\} \rangle|^2 \delta(E_{Ia} - E_{Fk}) \quad (2)$$

After replacing the Δ function by a step function of finite width, the rate constants can be obtained by summing over the Franck–Condon factors. This approach requires the calculation of Franck–Condon integrals and rapidly becomes prohibitive for large molecules and/or large energy differences between initial and final states. Instead of applying this time-independent approach, we opted here for the recently developed time-dependent approach to calculate the rate constants.[34] Fermi's golden rule is transformed to the Heisenberg picture, and the rate constants can be calculated from a straightforward time integration [Eq. (3)]:

$$k_{ISC} = \left| \left\langle \Phi_I | \hat{H}_{SO} | \Phi_F \right\rangle \right|^2 \int_{-\infty}^{\infty} dt G(t) e^{it(\Delta E_{IF} + (\frac{1}{2}) Tr \Omega_I)} \quad (3)$$

in which Ω_I is a matrix that contains vibrational frequencies of the initial state and $G(t)$ a time-dependent correlation function that contains information about the vibrational frequencies and normal coordinates of the initial and final states.[34]

Results

The discussion of our results is divided into three parts. In the first, we present the geometries and vibrational frequencies obtained with DFT calculations. The results are compared to experimental data of the LS state, and changes induced by the spin crossover are discussed. Secondly, we shortly review the CASPT2 calculations on the relative energies and spin–orbit coupling interactions of the different electronic states involved in the light-induced spin-crossover process. In the final part of this section, we quantify the rates of the deactivation channels and discuss the different mechanisms proposed for the photocycle of $[Fe(bpy)_3]^{2+}$.

DFT: Geometries and vibrational frequencies: In line with the conclusions drawn from several earlier studies, the PBE0/def2-TZVP geometry of the LS state is in excellent agreement with experimental data (see Table 1 as well as Figure 2). Except for a slight overestimation (0.03 Å) of the Fe–N distance, the calculated geometrical parameters are within 0.01 Å (distances) or 1° (angles) of the experimental estimates.[63] The DFT twist angle of the bipyridine ligand is slightly smaller than the experimental one. Given the short lifetime of the high-spin (HS) state, experimental information on the geometry of this state is more scarce. Time-resolved X-ray spectroscopy established that the Fe–N distance is (2.19 ± 0.04) Å in the HS state,[64,65] in agreement with the increase of 0.2 Å observed in many other Fe^{II} spin-crossover complexes. The PBE0/def2-TZVP calculations reproduce this increase in the Fe–N bond length in the HS state, which is 2.210 Å on average. Whereas the six Fe–N distances are equal for the LS case, there is a clear difference in the HS state. The ^3E state of the D_3-symmetry group is Jahn–Teller-active, and the distortion lowers the symmetry to C_2 with three Fe–N inequivalent distances in an interval of 0.02 Å around the average of 2.20 Å. The elongation of the Fe–N bonds is accompanied by a decrease in the N-Fe-N bite angle to release the strain in the ligand induced by the enlargement of the Fe coordination sphere. All other geometrical parameters remain practically the same as in the LS state.

In light of the observation that the largest geometry changes between the LS and HS states are related to the expansion of the FeN_6 unit, it is interesting to see how the frequencies of the Fe–N vibrational modes are affected by the spin crossover. A hypothetic isolated FeN_6 system of octahe-

Table 1. Selected distances [Å], angles [°], and dihedral angle [°] for $[Fe(bpy)_3]^{2+}$. The experimental structure is compared to the LS- and HS-optimized geometries.

	Exptl[63]	PBE0/def2-TZVP	
	LS	LS	HS
Fe–N1	1.967	1.996	2.190
Fe–N3	1.967	1.996	2.210
Fe–N5	1.967	1.996	2.198
N3–C1	1.338	1.335	1.332
N3–C2	1.359	1.348	1.342
C2–C3	1.470	1.467	1.479
N1-Fe-N2	81.9	80.9	74.7
N1-Fe-N3	94.3	95.2	95.7
N1-Fe-N4	174.6	174.6	166.6
N1-Fe-N5	94.3	95.2	96.8
N1-Fe-N6	89.8	88.9	93.8
Fe-N3-C1	127.6	126.6	125.0
Fe-N3-C2	115.0	115.0	116.0
C1-N3-C2	117.4	118.4	118.9
N3-C2-C3	114.0	114.6	116.1
N3-C2-C3-N4	6.4	2.6	5.5

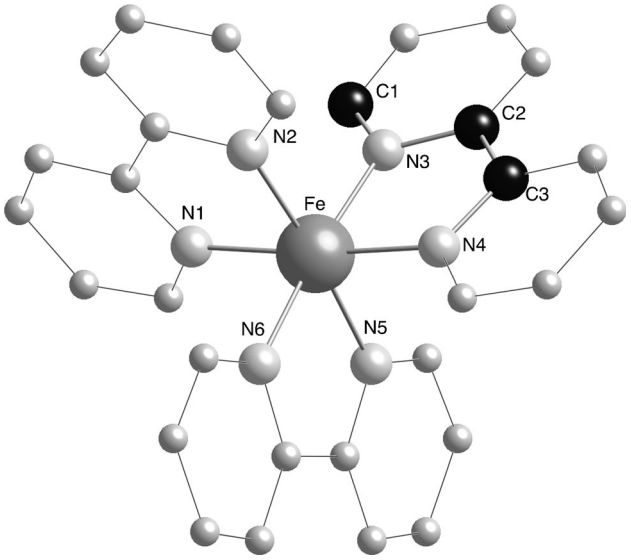

Figure 2. Labels of the atoms used in Table 1.

dral symmetry has six stretching (a_{1g}, e_g, t_{1u}) and nine bending (t_{1u}, t_{2u}, t_{2g}) vibrations. The fact that the symmetry of the real complex is lower than O_h and the observation that the Fe–N vibrations couple with ligand modes complicates the identification. Among the 177 different vibrational modes, the eighteen modes shown in Table 2 have the largest Fe–N

Table 2. Frequencies [cm^{-1}] of the Fe–N bending and stretching modes for the LS and HS states of $[Fe(bpy)_3]^{2+}$. The modes are labeled by the symbols of the D_3 and O_h (in parentheses) point groups and compared to experimental data for the LS state.

Character	LS	HS	Exptl[66]
Bending			
a_2 (t_{1u})	183.4	132.7	–
e (t_{1u})	205.8	149.6	–
e (t_{1u})	205.8	152.4	–
e (t_{2u})	231.4	195.1	242
e (t_{2u})	231.4	198.6	–
a_1 (t_{2u})	253.4	218.9	260
e (t_{2g})	276.6	241.9	276
e (t_{2g})	276.8	245.7	–
a_1 (t_{2g})	286.2	250.0	–
Stretching			
a_1 (a_{1g})	144.6	121.4	–
e (e_g)	170.2	116.2	–
e (e_g)	170.4	116.5	–
a_2 (t_{1u})	363.1	222.0	–
e (e_g)	370.2	358.0	–
e (e_g)	370.2	358.6	–
a_1 (a_{1g})	372.3	358.7	378
e (t_{1u})	378.7	251.9	390
e (t_{1u})	379.2	266.5	–

bending and/or stretching character. The stretching modes that originate from the a_{1g} and e_g octahedral modes (around 370 and 358 cm^{-1} for LS and HS, respectively) are strongly mixed with low-energy ligand vibrations at 145 (a_1) and 170 cm^{-1} (e) for the LS and 121 (a_1) and 116 cm^{-1} (e) for the HS, which are therefore included in Table 1. Owing to the strong mixing, the low-energy modes also show considerable Fe–N stretching character. Such mixing was previously observed in the analysis of the IR and Raman spectra by Alexander and co-workers.[66] The a_2 and e stretching modes that arise from the t_{1u} mode are characterized by an off-center movement of the central Fe^{II} ion, whereas the other three vibrations (a_1 and e) leave the Fe in the center of the cluster, thereby reflecting the gerade symmetry in O_h symmetry. The low-energy HS stretching modes of a_1 and e symmetry with calculated frequencies of 121 and 116 cm^{-1} provide a natural explanation for the 130 cm^{-1} oscillations observed by Consani et al.[25] The 220 cm^{-1} vibrational mode mentioned in the work of Consani et al. does indeed correspond to a Fe–N stretching vibration of the HS state, but is of different symmetry and implies an Fe off-center movement. The HS a_2 vibration with a calculated frequency of 133 cm^{-1} is an Fe–N bending mode and only weakly affects the Fe–N distance.

The comparison between LS and HS vibrational modes shows that the frequencies of the Fe–N are lower for the HS state, which is in line with previous reported experimental and theoretical studies.[36,66–69] The fact that the antibonding Fe 3d(e_g)-like orbitals become occupied with two electrons in the HS state weakens the Fe–N bond strength, thereby reverting to longer bond lengths and smaller stretching frequencies. Inelastic neutron scattering for related Fe^{II} complexes showed that the Fe–N bond-stretching frequency is reduced by approximately 50% on average. We did indeed observe such large reductions of the vibrational stretching for the a_2 and e modes that show Fe off-center movement, but much smaller weakening for the other modes.

CASPT2: Energetics and spin–orbit coupling: The linear interpolation between the HS- and LS-optimized geometries was taken as an approximate reaction coordinate of the light-induced spin-crossover process. A series of CASPT2 calculations was performed along this coordinate to construct the potential-energy surfaces of the lowest ligand-field and MLCT states. Formally these states have a Fe $3d^6$ (ligand-field) or Fe $3d^5$ L-π^{*1} (MLCT) electronic configuration, but the multiconfigurational treatment applied here introduces configurational mixing, and in some cases, especially for the higher-lying excited states, there is no clearly dominant contribution. The minimum in the $^1A_{1g}$ (LS) CASPT2 curve is located at a slightly smaller distance (1.927 Å) than the experimental value of 1.967 Å. This is a general feature of CASPT2 and is probably caused by neglecting the basis-set superposition error.[62] The MLCT states have similar minima as the $^1A_{1g}$, which is in agreement with the fact that none of the antibonding Fe 3d(e_g)-like orbitals is occupied. On the other hand, the minimum of the $^1T_{1g}$, $^3T_{1g}$, and $^3T_{2g}$ curves is displaced to longer Fe–N distances by approximately 0.1 Å. The dominant electronic configuration of the three states is Fe $3d(t_{2g}^5 e_g^1)$ (see Figure 3), and the electron in the antibonding orbital pushes the N atoms outwards. This effect is even larger in the $^5T_{2g}$ (HS) state. The leading configuration has two electrons in the Fe 3d(e_g) orbitals, and the minimum in the CASPT2 curve is located at 2.138 Å, which is approximately 0.2 Å longer than in the $^1A_{1g}$ state. The change from $S=0$ to $S=2$ due to the transfer of two

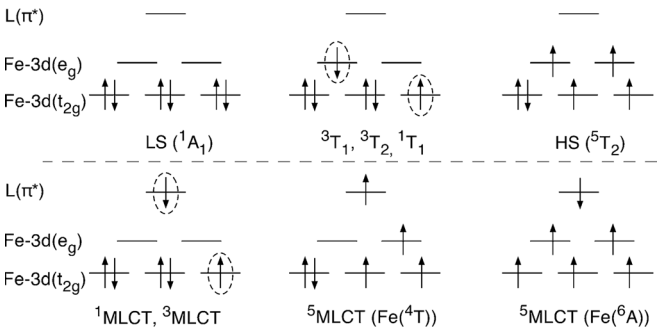

Figure 3. Schematic representation of the electronic configurations of the states discussed in the text. The encircled electrons are either low-spin or high-spin coupled to each other, depending on the total spin of the electronic state.

electrons from the nonbonding Fe 3d(t_{2g})-like orbitals to the antibonding Fe 3d(e_g)-like orbitals is accompanied by a charge transfer of approximately 0.5 electrons to the coordination sphere of the metal.[70]

Vertical and adiabatic energy differences are given in Table 3. The reference is the energy of the LS state in its CASPT2 equilibrium Fe–N distance. Taking this geometry as reference instead of the DFT-optimized geometry largely improves the relative energies of the ligand-field states.[29,38]

Table 3. Vertical and adiabatic CASPT2 energies [eV] of the low-lying electronic states of $[Fe(bpy)_3]^{2+}$.

State	Vertical	Adiabatic
$^1A_{1g}$	0.00	0.00
$^1T_{1g}$	2.61	2.30
$^3T_{1g}$	1.71	1.24
$^3T_{2g}$	2.26	1.76
$^5T_{2g}$	2.44	0.69
^{1}MLCT	2.51	2.51
^{3}MLCT	2.50	2.50

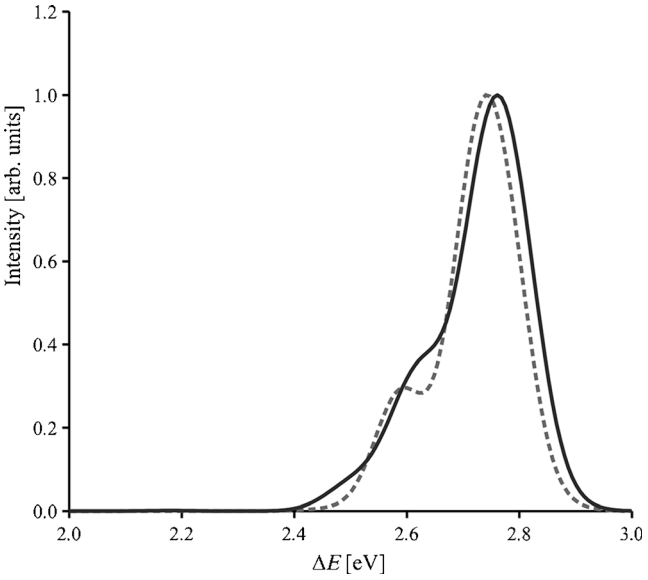

Figure 4. CASPT2 MLCT absorption spectra considering singlets only (dashed curve) and with singlet and triplet states (continuous curve). The calculations are performed at the CASPT2 Fe–N equilibrium distance. Each transition is represented with a Gaussian function with a full width at half-maximum (FWHM) of 0.15 eV.

This is easily understood by the schematic representation of the CASPT2 curves as function of the interpolation coordinate (see Figure 1). Whereas the $^1A_{1g}$ curve steeply rises with increasing Fe–N distance, the energy of the other ligand-field states is strongly reduced. The fact that the MLCT curves are nearly parallel to the $^1A_{1g}$ curve leads to a much weaker dependence of the vertical excitation energies for these states.

The energies given for the MLCT states correspond to the lowest transition energies—that is, the onset of the MLCT band—and do not give a measure of the position of the maximum of the band. The bottom of the MLCT band in the experimental absorption spectrum of $[Fe(bpy)_3]^{2+}$ was measured to lie at 600 nm, which corresponds to approximately 2.1 eV. This is slightly lower than the CASPT2 energies of the MLCT states given in Table 3. Furthermore, it is well established that the phosphorescence that involves ^{3}MLCT states takes place at energies that are approximately 0.2 eV lower than the fluorescence from the ^{1}MLCT states.[71] The results in Table 3 suggest that the calculations do not reproduce this 0.2 eV splitting between ^{1}MLCT and ^{3}MLCT, but it should be taken into account that this value only represents the onset of the band. Figure 4 compares the simulated MLCT band based on singlet states only (dashed line) to the one obtained including the ^{3}MLCT states in the calculation (solid line). Apart from a tiny shift in the position of the band maximum due to spin–orbit coupling effects, the major effect of including the ^{3}MLCT states in the description of the MLCT band is the rise in intensity at the low-energy side of the band. Analysis of the wavefunctions shows that in this energy interval many ^{3}MLCT states have important contributions from ^{1}MLCT states and hence gain some intensity. Hence, our calculations indeed indicate that the contribution of the triplet states to the MLCT band is maximal around energies 0.2 eV below the band maximum, which is in agreement with the conclusions derived from fluorescence and phosphorescence measurements.

The difference between experiment and theory in the position of the onset of the band arises from a combination of factors. In the first place, there is the precision of the theoretical procedure to calculate the excitation energies: experience has shown that CASPT2 reproduces excitation energies with a precision of about 0.15 eV in most cases. In the second place, there is the fact that our calculations are performed in a vacuum and not in solution as in the experimental work. However, the inclusion of solvent effects by the polarized continuum model (PCM) does not change the excitation energies. As long as the geometry of the complex is not changed, the MLCT excitation involves orbitals that are delocalized over the three ligands. Therefore the dipole moments in the ground and excited states do not change and solvent effects are practically zero.

A much larger effect is observed when the thermal motion of the nuclei is included in the description of the absorption spectra. For this purpose, we followed the strategy successfully applied for NiO and cytosine,[72,73] which consists of following the time evolution of the complex in a large box of water molecules[74–76] and then calculating the absorption spectrum at several snapshots along the molecular dynamics simulation. The loss of symmetry means that the three ligands are no longer equivalent at the different snapshots (as previously observed by Moret and co-workers in $[Ru(bpy)_3]^{2+}$[74]) although the average structure is compatible with the D_3-symmetry group extracted from the crystallographic data.[63] As a consequence of the symmetry breaking, the MLCT states involve electron replacements from the metal to one (or sometimes two) ligands, with sig-

nificantly lower excitation energy. The lowest MLCT states appear at 2.0 eV, which is in perfect agreement with the onset of an MLCT band. A more detailed description of the effect of the thermal motion and the symmetry breaking will be given in a future article.[77]

The spin–orbit coupling matrix elements were calculated for all low-lying N-electron states, including ligand-field and MLCT states. We considered the sixteen lowest states for each spin multiplicity, eight in each irreducible representation of the C_2-symmetry group. Taking into account the M_S degeneracy of the spin states, the spin–orbit coupling matrix has a dimension of 144×144, with nearly 4500 nonzero matrix elements. A selection of the spin–orbit couplings is given in Table 4. For each combination of low-lying electronic states the largest coupling is listed.

Table 4. Selected spin–orbit coupling matrix elements $\left\langle \Phi_I \middle| \hat{H}_{SO} \middle| \Phi_F \right\rangle$ of $[Fe(bpy)_3]^{2+}$ at d(Fe–N) = 1.93 Å, corresponding to the CASPT2 minimum distance for the LS state.

Φ_I	Φ_F	SO coupling [cm^{-1}]
^{1}MLCT	^{3}MLCT	199.9
^{1}MLCT	$^3T_{2g}$	214.3
^{1}MLCT	$^3T_{1g}$	96.0
^{3}MLCT	^{5}MLCT	344.3
^{3}MLCT	$^1T_{1g}$	164.7
^{3}MLCT	$^5T_{2g}$	6.2
^{3}MLCT	$^1A_{1g}$	81.6
$^3T_{2g}$	$^1T_{1g}$	131.4
$^3T_{2g}$	$^5T_{2g}$	219.9
$^3T_{2g}$	$^1A_{1g}$	83.7
$^3T_{1g}$	$^1T_{1g}$	75.5
$^3T_{1g}$	$^5T_{2g}$	417.7
$^3T_{1g}$	$^1A_{1g}$	527.7

As can be seen in Table 4, the couplings between the states largely vary. The simplification of using the (scaled) atomic spin–orbit coupling parameter of Fe ($\approx400\,cm^{-1}$) as an indication of the coupling between the states seems to be a rather crude approximation.[71] One of the most striking features is that the coupling between ^{3}MLCT and $^5T_{2g}$ is very small in comparison to the other couplings. This can be easily understood by looking at the dominant electronic configurations of the two states depicted in Figure 3. The orbital occupation differs by a double excitation, and hence there is no direct spin–orbit interaction. The nonzero value of the coupling arises from the admixture of other configurations to the total wavefunction of the two states. However, these contributions are too small to cause a substantial coupling.

Intersystem-crossing rates: The combination of the results discussed in the previous subsections (adiabatic energy differences, spin–orbit coupling matrix elements, and vibrational frequencies) gives us access to the transition rates of the intersystem crossings by means of the application of Fermi's golden rule rewritten in the time domain as explained above. In the following we will discuss the different steps (taking the ^{1}MLCT as the initial state) and subsequently investigate the different pathways toward the final HS ($^5T_{2g}$) state.

The ^{1}MLCT state can deactivate through an intersystem crossing to the ^{3}MLCT, $^3T_{1g}$, or $^3T_{2g}$ states (see Figure 1). The direct population of the HS state has to be disregarded due to the fact that there is no direct spin–orbit (SO) coupling between singlets and quintets. An effective coupling can in principle exist through second-order coupling that involves other excited states, but this effect is extremely small, as previously found for ligand-field states in $[Fe(tz)_6]^{2+}$ (tz = tetrazole).[29]

Given the rather high density of states at the bottom of the MLCT band, we have taken into account the four lowest ^{1}MLCT states in the determination of the decay rate. However, the results do not change substantially when only the lowest state is considered. The estimate for the ^{1}MLCT-to-$^3T_{2g}$ process increases from 23.5 to 44.6 fs. Since we only pursue to distinguish the order of magnitude of the different steps in the decay path, this difference is not really relevant. From the results in Table 5 it is clear that the ^{1}MLCT can not only decay extremely efficiently to the ^{3}MLCT state as previously suggested from experimental data, but also to the lower-lying $^3T_{2g}$ state. The latter state already has one electron transferred from a nonbonding Fe $3d(t_{2g})$ to an antibonding Fe $3d(e_g)$ orbital, whereas this is not the case in the ^{3}MLCT state. The details of the decay process between ^{1}MLCT and ^{3}MLCT are probably less relevant given the fact that these states have very similar energies and sizeable spin–orbit interaction. Therefore, the total spin is no longer a good quantum number, and the precise nature of these states is not clear as some of them appear to be a mixture of both spin states.

Table 5. Intersystem-crossing rates of the ^{1}MLCT state to other electronic states of $[Fe(bpy)_3]^{2+}$. The spin–orbit and vibrational contributions [see Eq. (3)] are given separately.

Φ_I	Φ_F	SO term [cm^{-2}]	Vibrational term [cm^2s^{-1}]	k_{ISC} [s^{-1}]	t [fs]
^{1}MLCT	^{3}MLCT	1.09×10^5	3.31×10^8	3.62×10^{13}	28
^{1}MLCT	$^3T_{2g}$	1.87×10^5	2.28×10^8	4.25×10^{13}	23
^{1}MLCT	$^3T_{1g}$	6.16×10^4	2.26×10^7	1.39×10^{12}	718

Table 6 summarizes the fate of the ^{3}MLCT state. This state can in principle undergo intersystem crossing to the excited ligand-field state $^1T_{1g}$ and the LS and HS states. Nevertheless, none of these pathways results in an intersystem-crossing rate that is compatible with the extremely short overall time of the deactivation. Hence, we conclude that the ^{3}MLCT undergoes an internal conversion to the $^3T_{2g}$. Unfortunately, no quantitative estimate of the timescale of this process can be given (yet), but considering the fact that the $^1MLCT\rightarrow{}^3T_{2g}$ process is extremely fast, the process with

Table 6. Intersystem-crossing rates of the ^{3}MLCT state to other electronic states of $[Fe(bpy)_3]^{2+}$. The spin–orbit and vibrational contributions [see Eq. (3)] are given separately.

Φ_I	Φ_F	SO term [cm^{-2}]	Vibrational term [cm^2s^{-1}]	k_{ISC} [s^{-1}]	t
^{3}MLCT	$^1T_{1g}$	3.91×10^4	3.48×10^6	1.36×10^{11}	7353 fs
^{3}MLCT	$^5T_{2g}$	2.25×10^2	3.20×10^7	1.39×10^{10}	>10 ps
^{3}MLCT	$^1A_{1g}$	3.36×10^3	7.91×10^5	2.66×10^9	>10 ps

Table 7. Intersystem-crossing rates of the $^1T_{1g}$, $^3T_{2g}$, and $^3T_{1g}$ states to other electronic states of $[Fe(bpy)_3]^{2+}$. The spin–orbit and vibrational contributions [see Eq. (3)] are given separately.

Φ_I	Φ_F	SO term [cm^{-2}]	Vibrational term [cm^2s^{-1}]	k_{ISC} [s^{-1}]	t
$^1T_{1g}$	$^3T_{2g}$	4.74×10^4	5.47×10^7	2.59×10^{12}	386 fs
$^1T_{1g}$	$^3T_{1g}$	1.73×10^4	2.11×10^7	3.65×10^{11}	2741 fs
$^3T_{2g}$	$^5T_{2g}$	8.64×10^4	1.57×10^6	1.35×10^{11}	7407 fs
$^3T_{2g}$	$^1A_{1g}$	2.92×10^3	1.41×10^5	4.14×10^8	>10 ps
$^3T_{1g}$	$^5T_{2g}$	2.11×10^5	7.61×10^7	1.61×10^{13}	62 fs
$^3T_{1g}$	$^1A_{1g}$	9.04×10^4	1.32×10^7	1.20×10^{12}	835 fs

similar initial and final states within the same spin manifold should be at least as fast.

The intersystem-crossing rates of the remaining ligand field states have also been calculated. The results are summarized in Table 7. As shown above, the first stage involves a rapid deactivation of the ^{1}MLCT to the $^3T_{2g}$ state, either directly or through the ^{3}MLCT. The second stage should involve the promotion of the second electron to the antibonding e_g orbital. This can be achieved by a direct deactivation from the $^3T_{2g}$ state to the $^5T_{2g}$ state. Despite the rather large SO contribution of this process, the vibrational term is not large enough to facilitate this path. The intersystem-crossing rate is two orders of magnitude smaller than needed for a process on femtosecond scale. The deactivation to the $^1A_{1g}$ is even slower. Hence, we conclude that the initial step (^{1}MLCT→(^{3}MLCT→)$^3T_{2g}$) is followed by an internal conversion (IC) from $^3T_{2g}$ to $^3T_{1g}$. The parallel nature of the potential-energy surfaces of these states shown in Figure 1 suggest that such a process is not favorable, but it should be kept in mind that this is only a schematic representation that reduces the vibrational motion of the complex to one dimension. To estimate the probability of the IC, we have calculated the vibrational contribution of the $^3T_{2g}$ to $^3T_{1g}$ conversion as was done for the ISCs. Taking into account all the vibrational modes leads to a vibrational coupling between the two states of 2.62×10^7 cm^2s^{-1}. This is, of course, only one ingredient of the coupling between the states (calculating the electronic coupling still remains to be done), but the vibrational part is not incompatible with a fast transition from $^3T_{2g}$ to $^3T_{1g}$. The second intersystem crossing from triplet to quintet when the second electron reaches the antibonding e_g orbitals is again very fast. Both the SO term and the vibrational contribution are large for the $^3T_{1g}$ to $^5T_{2g}$ crossing, thereby resulting in a time step of approximately 60 fs. The corresponding deactivation to the initial LS state is one order of magnitude slower, which is in agreement with the large quantum yield experimentally observed for the light-induced spin crossover. The branching ratio is 1:14, which means that in 93% of the transitions the HS state will be populated.

Discussion

Figure 5 provides a graphical summary of our results on the intersystem crossings in $[Fe(bpy)_3]^{2+}$. The ^{1}MLCT state can deactivate to the $^3T_{2g}$ state either directly through an intersystem crossing or through the ^{3}MLCT state. The latter two-step process involves a singlet–triplet intersystem crossing in the MLCT manifold, which is strongly favored by the spin–orbit coupling, and an internal conversion among triplet states. Both processes occur on the same timescale of approximately 30 fs. In this stage of the process, the Fe 3d(e_g) receives the first

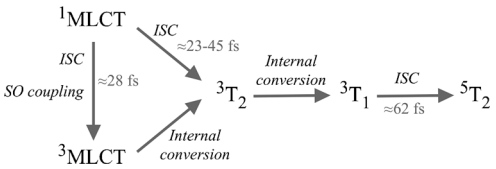

Figure 5. Summary of the photocycle of $[Fe(bpy)_3]^{2+}$ showing the deactivation of the ^{1}MLCT to the $^5T_{2g}$ state through several intermediate states.

electron. There is no fast intersystem crossing between the $^3T_{2g}$ state and the $^1A_{1g}$ or $^5T_{2g}$, and therefore the lower-lying $^3T_{1g}$ state is also involved in the deactivation process in the second stage. The $^3T_{1g}$ state is populated by an internal conversion from the $^3T_{2g}$ state and then deactivates rapidly ($\approx$60 fs) to the final HS state, accompanied by the occupation of the Fe 3d(e_g) orbitals with the second electron. The intersystem-crossing rate to the initial LS state is significantly slower.

The alternative of a direct deactivation from the ^{3}MLCT to the final HS state is attractive since it is compatible with experimental data and circumvents any possibility of population of the LS state. Despite the two states crossing in the Franck–Condon region, the fact that such direct transition requires the simultaneous movement of two electrons to occupy the Fe 3d(e_g) orbitals, one from the ligand π* orbital and the second from the Fe 3d(t_{2g}) orbitals, makes this scenario less probable from the theoretical point of view. The one-step mechanism is strongly hindered by the very small spin–orbit matrix element between the ^{3}MLCT and the $^5T_{2g}$ states. Note that this interaction is smaller than the one between the ^{3}MLCT and the $^1A_{1g}$ state (which differ by the transfer of only one electron), even when these states have a large energy separation.

The results discussed so far are subject to several approximations. In the first place, it is assumed that intersystem crossing only takes place from the lowest vibrational level of the initial state, or in other words, that vibrational cooling

(vc) is faster than intersystem crossing ($k_{ISC} < k_{vc}$). Given the short lifetimes of the intermediate states in the deactivation process, this assumption may not be completely satisfactory. Therefore, we extended the summation in Equation (2) to include higher vibrational levels in the initial state. The population of the vibrational levels follows a Boltzmann distribution with $T = 300$ K. In most cases, the vibrational contribution to the intersystem-crossing rate increases when excited vibrational levels are included in the summation. However, the increase is never larger than a factor of three, and the relative values remain practically the same as those listed in Tables 1–7 when only the lowest vibrational level of the initial state is considered. Although these results do not give a conclusive answer about the timescale of the vibrational cooling with respect to the intersystem crossing, they do indicate that the overall rate of the deactivation is not critically dependent on it. Both when $k_{ISC} < k_{vc}$ (deactivation from lowest vibrational level only) and $k_{ISC} \approx k_{vc}$ (deactivation from several vibrational levels), the overall timescale of the deactivation is on the same order of magnitude.

A second simplification in our calculation of the intersystem-crossing rates is the Condon approximation (i.e., the assumption that the spin–orbit coupling matrix elements are independent of the Fe–N distance). The values listed in Table 4 are calculated in the geometry that corresponds to the $^1A_{1g}$ CASPT2 equilibrium Fe–N distance. It is clear that not all the intersystem crossings take place at this geometry and that, strictly speaking, one should use different spin–orbit coupling matrix elements for the different crossings. To check the validity of the assumption, we also calculated the spin–orbit coupling at the Fe–N distance equal to 2.01 Å. As expected, the matrix elements among the ligand-field states are nearly identical in the two geometries. The spin–orbit coupling between $^3T_{1g}$ and $^1A_{1g}$ decreases from 527.7 cm^{-1} at the shorter distance (see Table 4) to 519.7 cm^{-1} at the larger Fe–N distance. For the other combinations of ligand-field states, similar variations of ± 10 cm^{-1} are observed. The variation in the matrix elements that involve MLCT states is slightly larger. For instance, the largest coupling between singlet and triplet coupled MLCT states is 199.9 cm^{-1} at the shorter distance and becomes 242.7 cm^{-1} upon expansion of the coordination sphere to 2.01 Å. However, the intersystem crossings that involve one or two MLCT states takes place at the initial stages of the deactivation process when no electron has yet been transferred to the antibonding e_g orbitals and the shorter Fe–N distances are more relevant. Moreover, the characterization of the electronic states as pure MLCT states becomes less relevant at larger distances, since important contributions from other electronic configurations (e.g., higher-lying ligand-field states) are observed in the wavefunction.

Finally, it can be argued whether or not the Fermi golden rule can be used to calculate the rate constants for such fast processes. It has been suggested that the deactivation process of light-induced spin crossover in Fe^{II} complexes is largely non-Born–Oppenheimer and that the conversion from ^{1}MLCT to $^5T_{2g}$ is intermediated by a collection of heavily mixed electronic states.[78,79] Indeed, the procedure described herein based on Fermi's golden rule should only be taken as a first rough picture of the deactivation dynamics. A more precise description should include nonadiabatic effects,[80] which can in principle be obtained from either surface-hopping dynamics[81–84] or by means of multiconfigurational time-dependent Hartree simulations.[85–88] However, such approaches are not easily applied to the present complex due the large number of atoms in the system and the consequently large number of degrees of freedom for the nuclear motion. At present, we are exploring the possibility of setting up a simplified vibronic-coupling model to study the nonadiabatic effects on the deactivation of the excited singlet state in $[Fe(bpy)_3]^{2+}$.

Conclusion

In conclusion, the outcomes of accurate ab initio electronic structure calculations (relative energies, geometries, and vibrational frequencies) have been used to study the dynamics of the light-induced magnetism in Fe^{II} complexes. The use of Fermi's golden rule results in a total timescale for the deactivation process that is in agreement with experimental estimates. The process involves a step-by-step mechanism in which the antibonding Fe 3d(e_g) orbitals become occupied one by one. The ligand-field triplet states play a fundamental role in the deactivation of the initially populated ^{1}MLCT state. We propose the following sequence for the photocycle: $^1A_{1g} \rightarrow {}^1\text{MLCT}(\rightarrow {}^3\text{MLCT}) \rightarrow {}^3T_{2g} \rightarrow {}^3T_{1g} \rightarrow {}^5T_{2g}$.

The experimental verification of the proposed deactivation scheme requires a time resolution on the order of 10 fs or better. X-ray measurements with free-electron lasers are approaching this precision but are generally not yet capable of detecting the intermediate ligand-field states due to the very low cross-sections. To obtain more detailed experimental insight into the photocycle in Fe^{II} complexes, there seems to be a need for a combined experimental/theoretical study on a complex with a slower deactivation process than the one observed in $[Fe(bpy)_3]^{2+}$ to facilitate the characterization of the intermediate states on the way from the initial excited singlet state to the final (metastable) HS state. Complexes with higher MLCT excitation energies might be good candidates for such studies.

Acknowledgements

Fruitful discussions with Wojciech Gawelda and Christian Bressler are gratefully acknowledged. Financial support has been provided by the Spanish Administration (projects CTQ2011-23140 and FIS2008-02238), the Generalitat de Catalunya (projects 2009SGR462, 2009SGR-1041, and Xarxa d'R+D+I en Química Teòrica i Computacional ((XRQTC)) and the European Union (COST Action CODECS CM1002). This work is part of the research program of the Foundation for Fundamental Research on Matter (FOM), which is part of the Netherlands Organisation for Scientific Research (NWO).

[1] O. Sato, J. Tao, Y.-Z. Zhang, *Angew. Chem.* **2007**, *119*, 2200; *Angew. Chem. Int. Ed.* **2007**, *46*, 2152.
[2] T. Miyamachi, M. Gruber, V. Davesne, M. Bowen, S. Boukari, L. Joly, F. Scheurer, G. Rogez, T. K. Yamada, P. Ohresser, *Nat. Commun.* **2012**, *3*, 938.
[3] R. Sessoli, D. Gatteschi, A. Caneschi, M. A. Novak, *Nature* **1993**, *365*, 141.
[4] M. Moragues-Cánovas, M. Helliwell, L. Ricard, E. Rivière, W. Wernsdorfer, E. Brechin, T. Mallah, *Eur. J. Inorg. Chem.* **2004**, 2219–2222.
[5] A. J. Tasiopoulos, A. Vinslava, W. Wernsdorfer, K. A. Abboud, G. Christou, *Angew. Chem.* **2004**, *116*, 2169; *Angew. Chem. Int. Ed.* **2004**, *43*, 2117.
[6] D. Gatteschi, R. Sessoli, F. Villain, *Molecular Nanomagnets*, Oxford University Press, Oxford, **2006**.
[7] O. Sato, T. Iyoda, A. Fujishima, K. Hashimoto, *Science* **1996**, *272*, 704.
[8] A. Bleuzen, C. Lomenech, V. Escax, F. Villain, F. Varret, C. Moulin, M. Verdaguer, *J. Am. Chem. Soc.* **2000**, *122*, 6648.
[9] J. M. Herrera, V. Marvaud, M. Verdaguer, J. Marrot, M. Kalisz, C. Mathonière, *Angew. Chem.* **2004**, *116*, 5584; *Angew. Chem. Int. Ed.* **2004**, *43*, 5468.
[10] X.-D. Ma, T. Yokoyama, T. Hozumi, K. Hashimoto, S.-I. Ohkoshi, *Phys. Rev. B* **2005**, *72*, 094107.
[11] M. Kozieł, R. Podgajny, R. Kania, R. Lebris, C. Mathonière, K. Lewiński, K. Krucza la, M. Rams, C. Labrugère, A. Bousseksou, *Inorg. Chem.* **2010**, *49*, 2765.
[12] H. Ma, J. L. Petersen, V. G. Young, Jr., G. T. Yee, M. P. Jensen, *J. Am. Chem. Soc.* **2011**, *133*, 5644.
[13] S. Venkataramani, U. Jana, M. Dommaschk, F. D. Sönnichsen, F. Tuczek, R. Herges, *Science* **2011**, *331*, 445.
[14] W. Gawelda, A. Cannizzo, V.-T. Pham, F. van Mourik, C. Bressler, M. Chergui, *J. Am. Chem. Soc.* **2007**, *129*, 8199.
[15] J. Jeftic, A. Hauser, *J. Phys. Chem. B* **1997**, *101*, 10262.
[16] C. de Graaf, C. Sousa, *Int. J. Quantum Chem.* **2011**, *111*, 3385.
[17] A. Hauser in *Spin Crossover in Transition Metal Compounds II, Vol. 234 of Topics in Current Chemistry* (Eds.: P. Gütlich, H. A. Goodwin), Springer, Heidelberg, **2004**), pp. 155–198.
[18] C. Bressler, C. Milne, V.-T. Pham, A. ElNahhas, R. M. van der Veen, W. Gawelda, S. Johnson, P. Beaud, D. Grolimund, M. Kaiser, *Science* **2009**, *323*, 489.
[19] C. Bressler, M. Chergui, *Annu. Rev. Phys. Chem.* **2010**, *61*, 263.
[20] A. Cannizzo, C. J. Milne, C. Consani, W. Gawelda, C. Bressler, F. van Mourik, M. Chergui, *Coord. Chem. Rev.* **2010**, *254*, 2677.
[21] G. Vankó, P. Glatzel, V.-T. Pham, R. Abela, D. Grolimund, C. N. Borca, S. L. Johnson, C. J. Milne, C. Bressler, *Angew. Chem.* **2010**, *122*, 6046; *Angew. Chem. Int. Ed.* **2010**, *49*, 5910.
[22] J. Tribollet, G. Galle, G. Jonusauskas, D. Deldicque, M. Tondusson, J.-F. Létard, E. Freysz, *Chem. Phys. Lett.* **2011**, *513*, 42.
[23] N. Huse, H. Cho, K. Hong, L. Jamula, F. M. F. de Groot, T. K. Kim, J. K. McCusker, R. W. Schoenlein, *J. Phys. Chem. Lett.* **2011**, *2*, 880.
[24] H. Cho, M. L. Strader, K. Hong, L. Jamula, E. M. Gullikson, T. K. Kim, F. M. F. de Groot, J. K. McCusker, R. W. Schoenlein, N. Huse, *Faraday Discuss.* **2012**, *157*, 463.
[25] C. Consani, M. Premont-Schwarz, A. ElNahhas, C. Bressler, F. van Mourik, A. Cannizzo, M. Chergui, *Angew. Chem.* **2009**, *121*, 7320; *Angew. Chem. Int. Ed.* **2009**, *48*, 7184.
[26] J. K. McCusker, K. N. Walda, R. C. Dunn, J. D. Simon, D. Magde, D. N. Hendrickson, *J. Am. Chem. Soc.* **1992**, *114*, 6919.
[27] A. Hauser, *J. Chem. Phys.* **1991**, *94*, 2741.
[28] P. Gütlich, Y. Garcia, H. A. Goodwin, *Chem. Soc. Rev.* **2000**, *29*, 419.
[29] B. Ordejón, C. de Graaf, C. Sousa, *J. Am. Chem. Soc.* **2008**, *130*, 13961.
[30] N. Suaud, M.-L. Bonnet, C. Boilleau, P. Labèguerie, N. Guihéry, *J. Am. Chem. Soc.* **2009**, *131*, 715.
[31] C. de Graaf, C. Sousa, *Chem. Eur. J.* **2010**, *16*, 4550.
[32] J. Chang, A. J. Fedro, M. van Veenendaal, *Phys. Rev. B* **2010**, *82*, 075124.
[33] M. van Veenendaal, J. Chang, A. J. Fedro, *Phys. Rev. Lett.* **2010**, *104*, 067401.
[34] M. Etinski, J. Tatchen, C. M. Marian, *J. Chem. Phys.* **2011**, *134*, 154105.
[35] J. Tatchen, N. Gilka, C. M. Marian, *Phys. Chem. Chem. Phys.* **2007**, *9*, 5209.
[36] M. Reiher, *Inorg. Chem.* **2002**, *41*, 6928.
[37] A. Fouqueau, M. E. Casida, L. M. Lawson Daku, A. Hauser, F. Neese, *J. Chem. Phys.* **2005**, *122*, 044110.
[38] K. Pierloot, S. Vancoillie, *J. Chem. Phys.* **2006**, *125*, 124303.
[39] S. Zein, S. A. Borshch, P. Fleurat-Lessard, M. E. Casida, H. Chermette, *J. Chem. Phys.* **2007**, *126*, 014105.
[40] J. Conradie, A. Ghosh, *J. Phys. Chem. B* **2007**, *111*, 12621.
[41] M. Swart, *J. Chem. Theory Comput.* **2008**, *4*, 2057.
[42] S. Ye, F. Neese, *Inorg. Chem.* **2010**, *49*, 772.
[43] R. Ahlrichs, M. Bär, M. Häser, H. Horn, C. Kölmel, *Chem. Phys. Lett.* **1989**, *162*, 165.
[44] TURBOMOLE V6.3 2011, a development of University of Karlsruhe and Forschungszentrum Karlsruhe GmbH, 1989–2007, TURBOMOLE GmbH, since **2007**; available from http://www.turbomole.com.
[45] C. Adamo, V. Barone, *J. Chem. Phys.* **1999**, *110*, 6158.
[46] J. P. Perdew, M. Ernzerhof, K. Burke, *J. Chem. Phys.* **1996**, *105*, 9982.
[47] F. Weigend, R. Ahlrichs, *Phys. Chem. Chem. Phys.* **2005**, *7*, 3297.
[48] E. Runge, E. K. U. Gross, *Phys. Rev. Lett.* **1984**, *52*, 997.
[49] R. Bauernschmitt, R. Ahlrichs, *Chem. Phys. Lett.* **1996**, *256*, 454.
[50] R. Bauernschmitt, M. Häser, O. Treutler, R. Ahlrichs, *Chem. Phys. Lett.* **1997**, *264*, 573.
[51] K. Andersson, P.-Å. Malmqvist, B. O. Roos, A. J. Sadlej, K. Wolinski, *J. Phys. Chem.* **1990**, *94*, 5483.
[52] Molcas 7.4 (**2009**), the following persons have contributed to the development of the MOLCAS software: K. Andersson, F. Aquilante, A. Bernhardsson, M. R. A. Blomberg, D. L. Cooper, M. Cossi, A. Devarajan, L. De Vico, N. Ferreé, M. P. Fülscher, A. Gaenko, L. Gagliardi, G. Ghigo, C. de Graaf, B. A. Hess, D. Hagberg, A. Holt, G. Karlström, J. W. Krogh, R. Lindh, P.-Å. Malmqvist, P. Neogrády, J. Olsen, T. B. Pedersen, J. Raab, M. Reiher, B. O. Roos, U. Ryde, B. Schimmelpfennig, L. Seijo, L. Serrano-Andrés, P. E. M. Siegbahn, J. Stålring, T. Thorsteinsson, V. Veryazov, P.-O. Widmark, and A. Wolf, http://www.molcas.org.
[53] F. Aquilante, L. De Vico, N. Ferré, G. Ghigo, P.-Å. Malmqvist, P. Neogrady, T. B. Pedersen, M. Pitonák, M. Reiher, B. O. Roos, *J. Comput. Chem.* **2010**, *31*, 224.
[54] B. O. Roos, R. Lindh, P.-Å. Malmqvist, V. Veryazov, P.-O. Widmark, *J. Phys. Chem. A* **2005**, *109*, 6575.
[55] K. Pierloot, S. Vancoillie, *J. Chem. Phys.* **2008**, *128*, 034104.
[56] M. Kepenekian, V. Robert, B. Le Guennic, C. de Graaf, *J. Comput. Chem.* **2009**, *30*, 2327.
[57] G. Ghigo, B. O. Roos, P.-Å. Malmqvist, *Chem. Phys. Lett.* **2004**, *396*, 142.
[58] N. Forsberg, P.-Å. Malmqvist, *Chem. Phys. Lett.* **1997**, *274*, 196.
[59] P.-Å. Malmqvist, B. O. Roos, *Chem. Phys. Lett.* **1989**, *155*, 189.
[60] P.-Å. Malmqvist, B. O. Roos, B. Schimmelpfennig, *Chem. Phys. Lett.* **2002**, *357*, 230.
[61] B. A. Hess, C. M. Marian, U. Wahlgren, O. Gropen, *Chem. Phys. Lett.* **1996**, *251*, 365.
[62] M. Pápai, G. Vankó, C. de Graaf, T. Rozgonyi, *J. Chem. Theory Comput.* **2013**, *9*, 509.
[63] S. Dick, *Z. Kristallogr. New Cryst. Struct.* **1998**, 213.
[64] W. Gawelda, V.-T. Pham, M. Benfatto, Y. Zaushitsyn, M. Kaiser, D. Grolimund, S. L. Johnson, R. Abela, A. Hauser, C. Bressler, *Phys. Rev. Lett.* **2007**, *98*, 057401.
[65] W. Gawelda, V.-T. Pham, R. M. van der Veen, D. Grolimund, R. Abela, M. Chergui, C. Bressler, *J. Chem. Phys.* **2009**, *130*, 124520.
[66] B. D. Alexander, T. J. Dines, R. W. Longhurst, *Chem. Phys.* **2008**, *352*, 19.

[67] H. Paulsen, H. Winkler, A. X. Trautwein, H. Grünsteudel, V. Rusanov, H. Toftlund, *Phys. Rev. B* **1999**, *59*, 975.
[68] J.-P. Tuchagues, A. Bousseksou, G. Molnár, J. J. McGarvey, F. Varret in *Spin Crossover in Transition Metal Compounds III, Vol. 235 of Topics in Current Chemistry* (Eds.: P. Gütlich, H. A. Goodwin), Springer, Heidelberg, **2004**, pp. 85–103.
[69] V. Legrand, S. Pillet, C. Carbonera, M. Souhassou, J.-F. Létard, P. Guionneau, C. Lecomte, *Eur. J. Inorg. Chem.* **2007**, *5693*–5706.
[70] M. Kepenekian, B. Le Guennic, V. Robert, *J. Am. Chem. Soc.* **2009**, *131*, 11498.
[71] M. Chergui, *Dalton Trans.* **2012**, *41*, 13022.
[72] A. Domingo, A. Rodríguez-Fortea, M. Swart, C. de Graaf, R. Broer, *Phys. Rev. B* **2012**, *85*, 155143.
[73] A. Domingo, A. Rodríguez-Fortea, C. de Graaf, *J. Chem. Theory Comput.* **2012**, *8*, 235.
[74] M.-E. Moret, I. Tavernelli, M. Chergui, U. Rothlisberger, *Chem. Eur. J.* **2010**, *16*, 5889.
[75] L. M. Lawson Daku, A. Hauser, *J. Phys. Chem. Lett.* **2010**, *1*, 1830.
[76] M. Swart, M. Güell, M. Solá, *Phys. Chem. Chem. Phys.* **2011**, *13*, 10449.
[77] A. Domingo, C. de Graaf, in preparation (2013).
[78] J. K. McCusker, K. N. Walda, R. C. Dunn, J. D. Simon, D. Magde, D. N. Hendrickson, *J. Am. Chem. Soc.* **1993**, *115*, 298.
[79] A. L. Smeigh, M. Creelman, R. A. Mathies, J. K. McCusker, *J. Am. Chem. Soc.* **2008**, *130*, 14105.
[80] D. R. Yarkony, *Chem. Rev.* **2012**, *112*, 481.
[81] A. W. Jasper, S. N. Stechmann, D. G. Truhlar, *J. Chem. Phys.* **2002**, *116*, 5424.
[82] C. Zhu, S. Nangia, A. W. Jasper, D. G. Truhlar, *J. Chem. Phys.* **2004**, *121*, 7658.
[83] G. Groenhof, L. V. Schäfer, M. Boggio-Pasqua, M. Goette, H. Grubmüller, M. A. Robb, *J. Am. Chem. Soc.* **2007**, *129*, 6812.
[84] M. E.-A. Madjet, O. Vendrell, R. Santra, *Phys. Rev. Lett.* **2011**, *107*, 263002.
[85] H.-D. Meyer, U. Manthe, L. S. Cederbaum, *Chem. Phys. Lett.* **1990**, *165*, 73.
[86] L. Blancafort, F. Gatti, H.-D. Meyer, *J. Chem. Phys.* **2011**, *135*, 134303.
[87] H.-D. Meyer, *WIREs Comput. Mol. Sci.* **2012**, *2*, 351.
[88] M. Moix Teixidor, F. Huarte-Larrañaga, *Chem. Phys.* **2012**, *399*, 264.

Received: July 30, 2013
Published online: November 7, 2013

